

Communication

Stacking-mode confined growth of 2H-MoTe₂/MoS₂ bilayer heterostructures for UV–vis–IR photodetectors

Yao Ding^{a,1}, Nan Zhou^{b,1}, Lin Gan^b, Xingxu Yan^{c,d}, Ruizhe Wu^a, Irfan H. Abidi^a, Aashir Waleed^f, Jie Pan^g, Xuewu Ou^a, Qicheng Zhang^a, Minghao Zhuang^a, Peng Wang^c, Xiaoqing Pan^{d,e}, Zhiyong Fan^f, Tianyou Zhai^{b,*}, Zhengtang Luo^{a,*}

^a Department of Chemical and Biomolecular Engineering, The Hong Kong University of Science and Technology, Clear Water Bay, Kowloon, Hong Kong

^b State Key Laboratory of Material Processing and Die and Mould Technology, School of Materials Science and Engineering, Huazhong University of Science and Technology, Wuhan 430074, PR China

^c National Laboratory of Solid State Microstructures, College of Engineering and Applied Sciences and Collaborative Innovation Center of Advanced Microstructures, Nanjing University, Nanjing 210093, PR China

^d Department of Chemical Engineering and Materials Science, University of California-Irvine, Irvine, CA 92697, USA

^e Department of Physics and Astronomy, University of California-Irvine, Irvine, CA 92697, USA

^f Department of Electronic and Computer Engineering, The Hong Kong University of Science and Technology, Clear Water Bay, Kowloon, Hong Kong

^g Department of Physics, The Hong Kong University of Science and Technology, Clear Water Bay, Kowloon, Hong Kong

ARTICLE INFO

Keywords:

Heterostructures
Chemical vapor deposition
Photodetectors
MoTe₂
P-n junctions

ABSTRACT

The atomic thin, vertically-stacked 2H-MoTe₂/MoS₂ heterostructures are successfully synthesized using the single step chemical vapor deposition (CVD) method and a magnet-assisted secondary precursor delivery tool. The second material (MoTe₂) was grown in a well-controlled, unique and epitaxial 2H-stacking mode atop the first material (MoS₂), starting from the edges. This led to the construction of a vertical p-n junction with a broadband photoresponse from the ultraviolet (UV, 200 nm) to the near-infrared (IR, 1100 nm) regions. The high crystallinity of MoTe₂/MoS₂ heterostructures with a modulation of sulfur and tellurium distribution is corroborated by multiple characterization methods, including Raman spectroscopy, photoluminescence (PL) spectroscopy and high-angle annular dark field scanning transmission electron microscopy (HAADF-STEM). Furthermore, the photoelectrical measurements exhibit a tremendous photoresponsivity with an external quantum efficiency (EQE) as high as 4.71 A/W and 532% at 1100 nm, while as 4.67 A/W and 1935% at 300 nm, one to two orders of magnitude higher than other exfoliated MoTe₂ heterostructure devices have been reported so far. This synthetic method is a controllable stacking mode confined synthesis approach for 2D heterostructures, and paves the way for the fabrication of high-performance functional telluride-based broadband photodetectors.

1. Introduction

Transition-metal dichalcogenides (TMDs), a new series of two-dimensional (2D) semiconductors beyond graphene and hexagonal boron nitride (h-BN), due to their exceptionally novel optical properties [1–3], have great potential to be the basic building block for a wide range of applications, such as optoelectronic devices, catalysis, energy storage and biomedicines. More importantly, van der Waals (vdWs) heterostructures, which include two or more kinds of 2D materials stacked vertically, have shed light on the physics of modern semiconductors because of the possibility of the formation of the secondary Dirac points

[4], bandgap opening [5] and surface reconstruction by commensurate-incommensurate transition in system [6]. To utilize the extraordinary physical properties of TMDs, the construction of heterostructures is a prerequisite. Stacking different 2D materials by mechanical exfoliation and transfer techniques is a simple way to obtain vdWs heterostructures [7]. However, imperfect stacking and interface contamination caused by the transfer and the subsequent degradation of the quality of heterostructures [8] is inevitable. Several recent reports have shown that vdWs heterostructures of the layered TMDs, such as WSe₂/MoSe₂ [9], MoS₂/WSe₂ [10] and WS₂/MoS₂ [11], which were synthesized under the chemical vapor deposition (CVD) method, realize a much better

* Corresponding authors.

E-mail addresses: zhaity@hust.edu.cn (T. Zhai), keztluo@ust.hk (Z. Luo).

¹ Y. Ding and N. Zhou contributed equally to this work.

well-defined stacking mode and clean interface, thus circumventing the problems encountered with the transfer method.

Recently, molybdenum ditelluride (MoTe_2) has attracted great interest due to its moderate optical band gap (1.1 eV for monolayer) that can potentially extend the photoresponse from the ultraviolet to the near-infrared range [12]. Although the monolayer 1 T' metallic phase MoTe_2 has been successfully synthesized using the CVD method [13], the direct growth of the 2 H semiconductor phase MoTe_2 -based heterostructures with other layered TMDs of high quality still remains a big challenge. This has not yet been achieved, probably due to the assisted role of Te in the low-temperature synthesis of TMDs [14,15] and the instability of pure MoTe_2 in the atmosphere [16]. The atom exchange strategy has been employed to transform monolayer MoS_2 into MoTe_2 but, unluckily, with a multiphase [17]. Additionally, despite the fact that a few layers of vertically stacked $\text{MoTe}_2/\text{MoS}_2$ vdWs heterostructures can be fabricated using molecular beam epitaxy (MBE), the obtained products are of imperfect crystalline structures and extremely low yield, and is therefore difficult to mass produce practical applications [18].

In this work, we demonstrated the preparation of highly crystallized

$\text{MoTe}_2/\text{MoS}_2$ vdWs heterostructures using a magnet-assisted precursor delivery CVD system in which the precursor supply can be accurately switched during growth. As a result, the $\text{MoTe}_2/\text{MoS}_2$ heterostructures were fabricated by direct all-CVD growth without any intermediate transfer steps. The Raman spectra revealed a clear spatial distribution of MoTe_2 and MoS_2 in the heterostructures, as shown by the mapping of the peak position. The heteroepitaxial MoTe_2 preferred to *in situ* grow atop and along the edges of the MoS_2 . High-angle annular dark field (HAADF) STEM imaging with atomic resolution revealed that MoTe_2 was perfectly grown on the top of MoS_2 with 2H-stacking mode. Photoluminescence (PL) unveiled the charge transfer between MoTe_2 and MoS_2 layers, which resulted in a distinct PL quenching in the overlapped area. Furthermore, optoelectronic transport measurements demonstrated that the heterostructures were high-performance p-n diodes with a clear photovoltaic effect in the wide regions, ranging from ultraviolet (200 nm) to near-infrared (1100 nm). This work achieved and improved the expected positive performance reported by previous works [19,20,39]. In addition, such a facile synthesis route to achieve $\text{MoTe}_2/\text{MoS}_2$ heterostructures with remarkable optoelectronic properties makes it a promising candidate for use in diverse applications,

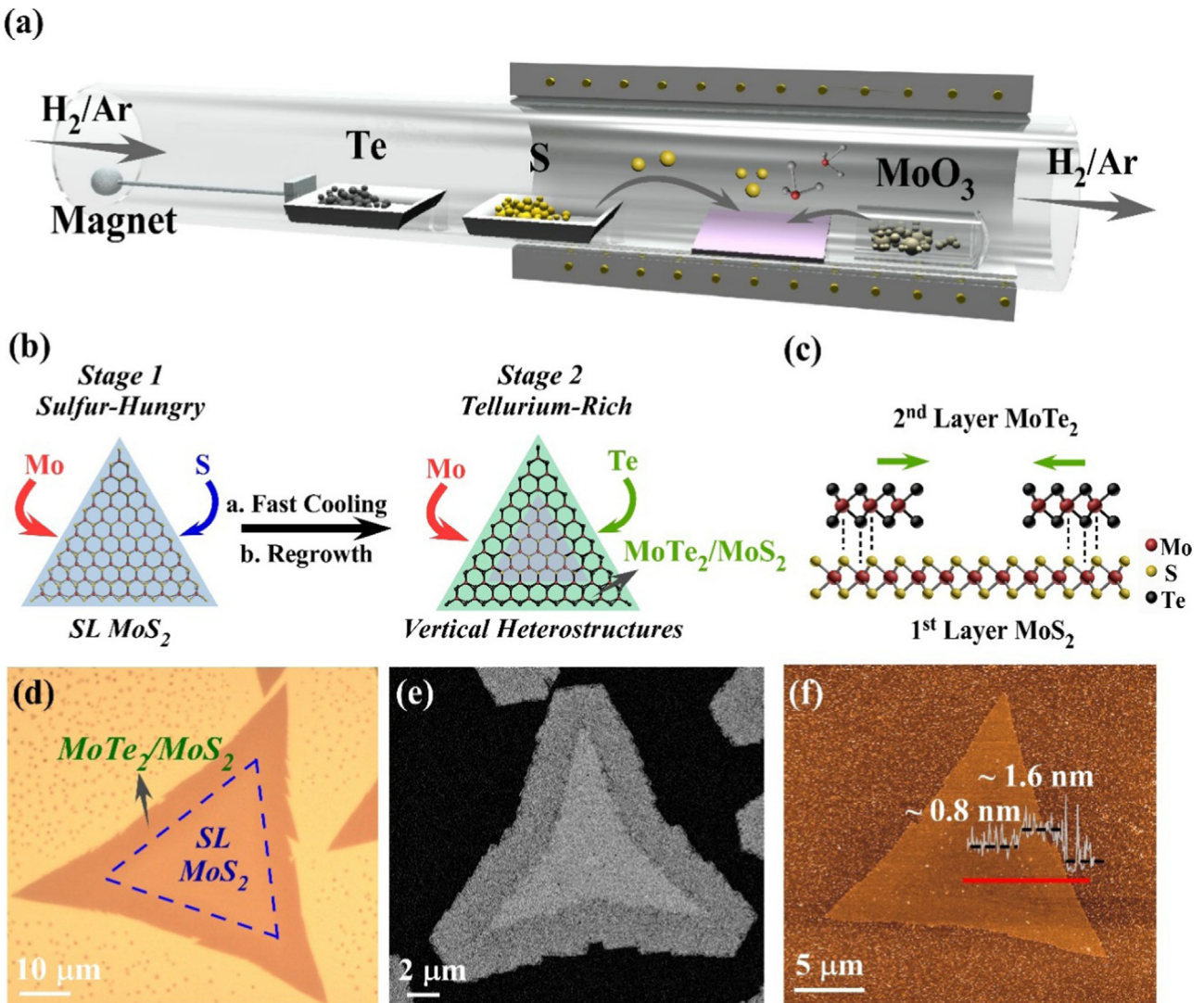


Fig. 1. Experimental schematic diagram and overall morphologies of the vertically stacked $\text{MoTe}_2/\text{MoS}_2$ heterostructures. (a) Setup of the magnet-assisted CVD quartz tube. (b) The under layer MoS_2 was grown in the first stage. After fast cooling and regrowth, Te gas was introduced in the second stage. The crystal forms a vertically stacked $\text{MoTe}_2/\text{MoS}_2$ heterostructure. (c) Schematic side view of the $\text{MoTe}_2/\text{MoS}_2$ heterostructures. (Mo atoms are shown in red, S are yellow, Te are black) (d) Optical image of the $\text{MoTe}_2/\text{MoS}_2$ heterostructure. (e) Backscattered SEM image of the $\text{MoTe}_2/\text{MoS}_2$ heterostructure. (f) AFM characterization of the same flake in (d), showing a center region with a thickness of 0.8 nm and an outside region with a thickness of 1.6 nm.

especially for near-infrared photodetectors and solar cells.

2. Results and discussions

Fig. 1a shows the schematic of the synthesis process for MoTe₂/MoS₂ heterostructures using the magnet-assisted CVD method. We used a scalable single-run CVD process by precisely controlling the additional time and amount of chalcogenides precursors introduced during the growth. More details are provided in the [Experimental section](#). A magnet with one side attached to a quartz boat was used to deliver the tellurium powder into the heating zone of a one-inch quartz tube furnace when needed. The furnace was on the sliding rails that helped it move horizontally. The whole growth process remained at ambient pressure. Here, we followed an established method [53], which was observed to obtain larger MoS₂ flakes/heterostructures than if MoO₃ were loaded on the upstream side. This method normally increases the dwelling time of the MoO_{3-x} intermediate, eventually leading to an increased flake size. Before growth, the system was pumped and refilled with pure Ar (500 sccm) for 5 min to exclude oxygen. The furnace was then heated to 780 °C at a heating rate of 40 °C/min. In this method, the pure and clean SiO₂/Si was chosen as the growth substrate because it can *in situ* get the surface clean photovoltaic (PV) devices on chip without any transfer processes that will result in contamination and further promote the PV behavior. As shown in **Fig. 1b**, the growth process can be divided into two stages: (1) the growth of MoS₂ seeds at 780 °C for 10 min using 30 sccm Ar as carrier gas; and (2) continued epitaxial growth of MoTe₂ at 680 °C for 10 min using 30 sccm Ar and 3 sccm H₂ after fast cooling and regrowth with tellurium powder loading. When the first stage was finished, a high flowrate of Ar (500 sccm) was quickly introduced into the tube to blow away the remaining sulfur atmosphere. At the same time, the temperature was reduced and the furnace was slid downstream to quickly cool the samples. After 2 min, the substrate was reheated to 680 °C and the second stage began. In the first stage, a “sulfur-hungry” environment (MoO₃: Sulfur = 8: 1, weight ratio) was used to grow the MoS₂ seeds to consume all the sulfur, since extra sulfur is deleterious to the formation of MoTe₂ in the second stage of growth [14,21]. Our control experiment demonstrated that it is difficult to synthesize MoTe₂/MoS₂ heterostructures in a sulfur-rich environment. Instead only MoS₂ formed while using a large amount of sulfur (40 mg), as shown in **Fig. S1**. Furthermore, other evidence, such as the appearance of spiral shaped MoS₂ on the surface of the heterostructures (**Fig. S2**), can be identified as the “sulfur-hungry” feature during stage one, similar to previous results under the condition of insufficient sulfur supply [22]. After the formation of MoS₂ seeds in the first stage, a fast cooling process with high Ar flowrate was applied to purge the chamber before the introduction of tellurium powder. After the loading of tellurium powder into the heating zone, MoTe₂ continued to grow along the edges of existing MoS₂ seeds. **Fig. 1c** schematically illustrates the formation of these vertically stacked MoTe₂/MoS₂ heterostructures during the second stage, in which MoTe₂ grew over the first single-layer (SL) MoS₂ from the edge nucleation and epitaxially grew to the center area to form a vertically stacked MoTe₂/MoS₂ heterostructure with a SL MoTe₂ ring as the upper layer and a SL MoS₂ as the under layer. This growth mechanism is similar to what has been explained in other TMDs heterostructures [3,23]. **Fig. 1d** shows the optical image of a typical MoTe₂/MoS₂ heterostructure domain obtained by following our method, with more optical images shown in **Fig. S3**. The synthesized triangular shaped heterostructures clearly exhibit two concentric domains with a core-ring structure, although their shapes can be standard triangles, truncated triangles or hexagons. The contrast across the interface can be seen in the backscattered scanning electron microscopy (SEM) images, as shown in **Fig. 1e** (more details see **Fig. S4**). Principally, for backscattered SEM images, the material with a higher molecular weight should reflect more electrons than the lighter one, and thus MoTe₂ should be brighter than MoS₂. However, in our case, MoTe₂ is epitaxially grown on the MoS₂ surface with an

ultraclean interface that has few electron traps. Oppositely, MoS₂, which is directly grown on the SiO₂/Si substrate, may contain many electron traps at the interface that can enhance the brightness of MoS₂ in backscattered SEM characterization. Therefore, the upper MoTe₂ layers finally behave as the darker material, as compared with the under MoS₂ layers. In addition, during the synthesis process, the growth of MoTe₂ may also be affected by the diffusion. However, this only exists as an atomic substitution within a small range, so will not dramatically influence the photovoltaic behavior of the heterostructures. If we elongate the MoTe₂ growth time, the second MoTe₂ layer will also cover the surface of the center zone of MoS₂, as shown by **Fig. S4d**. This is consistent with the previous report [9]. To determine the thickness of the heterostructures, atomic force microscopy (AFM) was used to characterize the height differences between the center and outside regions. **Fig. 1f** displays the height image of a triangular MoTe₂/MoS₂ heterostructure domain on the SiO₂/Si substrate, showing a center region with a thickness of 0.8 nm and an outside region with a thickness of 1.6 nm. This result further indicates that the center area is a SL MoS₂ while the outside is a vertically stacked bilayer MoTe₂/MoS₂ heterostructure.

Raman and PL spectroscopy were adopted to map the obtained heterostructures. As shown in **Fig. 2a** and **b**, the characteristic resonance peaks of monolayer MoS₂, i.e. the out-of-plane A_{1g} mode at 400 cm⁻¹ and the in-plane E_{2g}¹ mode at 380 cm⁻¹, are observed in the inner core region, while the characteristic in-plane E_{2g}¹ peak at around 240 cm⁻¹ [24,25] of 2H-phase MoTe₂ is detected only in the ring area. Here, no 1T'-phase MoTe₂ was found on top of the MoS₂ in any of the tested samples and flakes. There is a slight redshift (from 380 cm⁻¹ to 375 cm⁻¹) of the E_{2g}¹ peak for MoS₂ in the ring area, probably due to the large stretching stress from the upper layer MoTe₂ [26] which has a much large lattice parameter ($a = 3.519 \text{ \AA}$ [27]) than MoS₂ ($a = 3.16 \text{ \AA}$ [28]). It is worth noting that this large E_{2g}¹ peak downshift has not been observed in previous reports, which used artificial exfoliated MoTe₂ stacked with MoS₂, demonstrating a good contact between the SL MoTe₂ and MoS₂ produced using our CVD-based method. Besides, for the MoS₂ in the inner core region, there is also a non-uniform redshift for the E_{2g}¹ peak. This non-uniform redshift is probably due to lattice deformation which is caused by the outside MoTe₂/MoS₂ bilayers [29]. Corresponding with the downshift of the E_{2g}¹ peak for MoS₂ is also an upshift of the E_{2g}¹ peak for MoTe₂ in the ring region. This is in comparison with the SL MoTe₂ on the bare SiO₂/Si substrate [30], due to the compression stress from the under layer MoS₂. Only 2H-phase MoTe₂, which is more thermodynamically stable than the 1T'-phase MoTe₂ [2,23,31], was obtained. The core-ring structure of these vertically stacked MoTe₂/MoS₂ heterostructures was further confirmed by the results of Raman mapping of 240 cm⁻¹ of MoTe₂, 380 cm⁻¹ and 375 cm⁻¹ for MoS₂, as can be seen in **Fig. 2c-f**. **Fig. 2g** illustrates the PL spectra taken from the separated regions in a MoTe₂/MoS₂ heterostructure. Emission peaks of the MoS₂ were observed in the core area of the flake at 640 and 690 nm, corresponding to the B and A direct excitonic transition of the near band-edge emission [32], respectively. The A peak for MoS₂ had a dramatic quenching in the ring region of the flake, as shown by the PL intensity mapping at 690 nm in **Fig. 2h**. In addition, the PL peak at 1.1 eV [33], known as the emission peak for MoTe₂, is not observed here. This PL quenching for both the SL MoS₂ and SL MoTe₂ in the heterojunction area can be illustrated by the charge separation mechanism in **Fig. 2i**. When a SL MoS₂ (with a direct band gap of 1.8–1.9 eV) was stacked with a SL MoTe₂ (with a direct band gap of 1.05–1.1 eV), the interlayer coupling interaction between MoTe₂ and MoS₂ resulted in a type II staggered band alignment [33]. Under the laser illumination, electrons will be transferred from the conduction band of MoTe₂ to the conduction band of MoS₂, and oppositely, holes will be transferred from the valence band of MoS₂ to that of MoTe₂. This interlayer charge separation and energy band alignment can conduct the PL quenching in the MoTe₂/MoS₂ hetero-stacking regions, as has been found in other bilayer TMDs heterostructures [34].

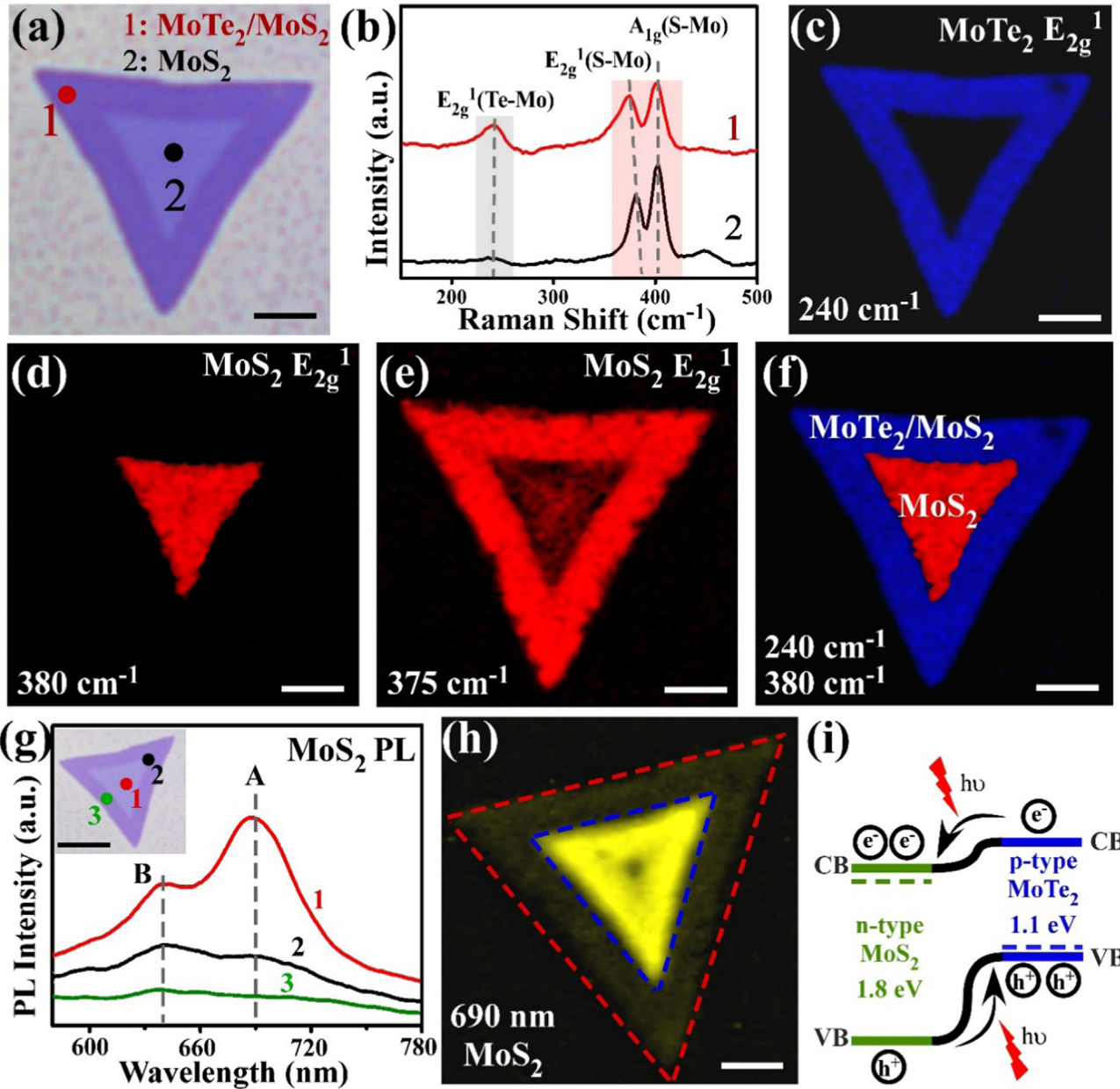


Fig. 2. Raman and photoluminescence (PL) characterization of the MoTe₂/MoS₂ heterostructures. (a) Optical image of the tested flake in (b–f). (b) Raman spectra collected at the points marked in (a). (c–e) Raman intensity mapping images at different Raman shifts for MoS₂ and MoTe₂. (240 cm^{-1} for (c), 380 cm^{-1} for (d) and 375 cm^{-1} for (e), respectively) (f) Combined Raman intensity mapping at 240 cm^{-1} (blue) and 380 cm^{-1} (red). Scale bars in (a–f), 3 μm . (g) PL spectra of MoS₂ in the center, interface and outside area as marked in inset, shown a direct band (690 nm) quench for MoS₂ in the outside area. Inset: optical image of the heterostructure used for PL characterization. Scale bar, 10 μm . (h) PL intensity mapping at 690 nm. Scale bar, 3 μm . The red dash lines outline the heterojunction and the blue dash lines show the interface of the inner core and outside ring regions. (i) The idea energy band diagram at the vertically stacked junction area between MoS₂ and MoTe₂ under illumination.

However, we did not detect any new PL peak of the inter-band transition for our MoTe₂/MoS₂ heterostructures. To further identify the elemental composition and the bonding nature of MoTe₂/MoS₂ heterostructures, X-ray photoelectron spectroscopy (XPS) was also performed, as shown in Fig. S6.

In order to prove that the heterostructures were epitaxially grown in nature, we performed a high-angle annular dark field (HAADF) STEM and further explored the crystallinity of the MoTe₂/MoS₂ heterostructures, as shown in Fig. 3. On the Z-contrast image in Fig. 3a, the interface of a SL MoTe₂ and a SL MoS₂ is clearly identified, showing that the atomically thin SL MoTe₂ was grown from the edges of the MoS₂ domains. The inset in Fig. 3a shows the morphology of the as-transferred stacked MoTe₂/MoS₂ heterostructure in a low-

magnification image. The step edge between the under MoS₂ SL and upper MoTe₂/MoS₂ bilayer is discernable in Fig. 3a, showing that a bilayer MoTe₂/MoS₂ exhibits a higher image contrast than a SL MoS₂. Notably, the selected area electron diffraction (SAED) patterns (Fig. 3b and c) collected from the different regions in the junction area show dramatic differences. Also, it is noted that the SAED from the SL MoS₂ area shows only one set of diffraction pattern while the SAED from the bilayer (BL) MoTe₂/MoS₂ area shows two different sets of diffraction patterns. The results show that one set of the points corresponds to the MoTe₂ lattice ($a = 3.519 \text{ \AA}$) and the other corresponds to the MoS₂ lattice ($a = 3.16 \text{ \AA}$), further indicating that the bilayer regions are two individual materials rather than uniform $\text{MoS}_{2x}\text{Te}_{2(1-x)}$ alloys. Fig. 3d shows a zoom of the Z-contrast image from the bilayer region. The

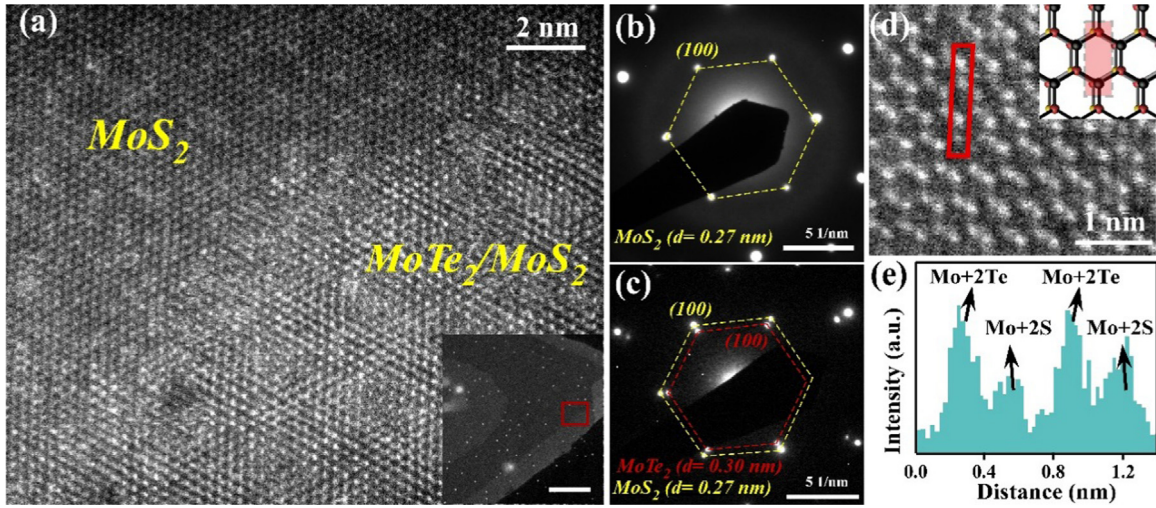


Fig. 3. HAADF-STEM characterization of lateral interface of the vertically stacked MoTe₂/MoS₂ heterostructure. (a) atomic-resolution Z-contrast STEM image of the junction area marked with a red rectangle in the inset image. Inset: low-magnitude STEM image of the MoTe₂/MoS₂ vertically stacked heterostructure. Scale bar of the inset, 1 μm. (b) & (c) SAED patterns collected from two different regions, MoS₂ SL and MoTe₂/MoS₂ BL, respectively, in (a). (d) Zoom in Z-contrast image of the vertically stacked junction area. Inset: schematic of the 2H-stacking in the vertically stacked MoTe₂/MoS₂ heterostructure. The atoms in the red rectangles of (d) and its inset correspond to each other. (e) Image intensity profile acquired along the red rectangle in (d).

alternative bright and dark atoms arrangement in the hexagonal lattice suggests the MoTe₂/MoS₂ heterostructure is in a 2H-stacking mode (schematic shown in Fig. 3d inset). Different from the artificially stacked heterostructures, this preserved 2H-stacking mode in our CVD-based synthesized heterostructures exemplifies the advantage of our growth method, where the stacking orientation can be well controlled.

Moiré pattern, which is commonly seen in the vertical stacking of two different 2D materials due to a large lattice mismatch [36], is also observed in our MoTe₂/MoS₂ heterostructures shown in Figs. 4a and 4b. The lattice mismatch between MoTe₂ and MoS₂ is 10.2%, according to the formula,

$$\epsilon = \frac{a_{\text{MoTe}_2} - a_{\text{MoS}_2}}{a_{\text{MoTe}_2}} \times 100\%$$

where a_{MoTe_2} and a_{MoS_2} are the lattice constant of MoTe₂ and MoS₂, respectively. Fig. 4b presents the atomic resolution Z-contrast STEM image of one junction area of MoTe₂/MoS₂ heterostructure, from which the periodicity of one Moiré pattern was estimated to be 2.3 nm, indicating the formation of a periodic superlattice. By measuring the atomic intensity along the red arrow in Fig. 4b of the heterojunction area (Fig. 4c), the layered heterostructure, which is one layer of MoTe₂ on top of one layer of MoS₂ was verified. This is consistent with the observation in Fig. 3. In order to simulate the Moiré pattern in Fig. 4b, a schematic top view of the layered MoTe₂/MoS₂ heterostructure was built, as shown in Fig. 4d. By mimicking the atomic structure of the heterojunction in proportion to the lattice constant (0.316 Å/unit), we found that every seven units can form a periodic Moiré pattern. That is, the periodical length is around 2.21 nm, which is consistent with the measurement noted in Fig. 4b.

The above discussion clearly demonstrates the successful growth of vertically stacked MoTe₂/MoS₂ heterostructures. Based on these structural characterizations, it can be proposed that the atomically thin p-n diode based on this vertical heterojunction between synthetic p-type MoTe₂ and n-type MoS₂ will be formed. To evaluate the electron transport and optical properties, the photovoltaic devices of MoTe₂/MoS₂ heterostructures on pure, clean SiO₂/Si substrate were fabricated using standard electron beam lithography (EBL). Here, the growth temperature was maintained at $< 800^\circ\text{C}$, which only slightly degraded the SiO₂, as it was observed that such effect became significant at $> 900^\circ\text{C}$ [55]. To further minimize the SiO₂ degradation, after transfer, we annealed the sample at a relatively low temperature

($< 200^\circ\text{C}$). The optical image of a single MoTe₂/MoS₂ heterostructure device is depicted in the inset of Fig. 5a. To electrically access the inner MoS₂ triangles without shorting to the outside MoTe₂ peripheral layers, a partial etching of the MoTe₂/MoS₂ heterostructures was prepared in advance before writing the electrodes. A thin film of PMMA was firstly spin-coated onto the as-received sample. After this first exposure, only half of the wanted flakes was protected by PMMA while the rest was lifted off by lithography. By this method, one electrode can be contacted to the p-type MoTe₂ while the other can be contacted to the MoTe₂/MoS₂ bilayer in the electrodes writing step. The electrodes were made by depositing 10 nm Cr/50 nm Au thin films as the contacts (details are in the Characterization section and Fig. S8). We employed Cr/Au as the electrode for both materials for two reasons. Firstly, the Fermi level of MoTe₂ and MoS₂ are ~ -4.3 eV and ~ -5.1 eV [48], while the work function of Cr is ~ -4.6 eV, which just met the requirement of Ohmic contact. Secondly, Cr/Au electrode is the most adopted electrode in reported literature due to its ability to contact well to many kinds of materials. Fig. 5a plots the calculated spectral responsivities of heterostructures with an incident light from 300 nm to 1100 nm, as a function of wavelength. The calculations followed the equation:

$$\text{Responsivity}(R) = \frac{I_{ph}}{P \times A},$$

where I_{ph} is the generated photocurrent $I_{ph} = I_{light} - I_{dark}$; P is the incident light power density; and A is the active illuminated area of the device. According to the plot, the laser with 1100 nm shows the highest responsivity value of about 4.71 A/W with light power density of 4.209 mw/cm² (details in Table S1). The external quantum efficiency (EQE, %) plots of the 2D MoTe₂/MoS₂ p-n diodes shows the same tendency as their responsivity behavior (Table S1), with the highest EQE as 1.935 $\times 10^{3\%}$ at 300 nm illumination. These values were compared with other heterostructures used as photovoltaic materials, as shown in Table 1. Compared with the previous vertical heterostructures provided by exfoliation [19,20,41–45] or two-steps CVD [46,47,54,56], our heterostructures show a photoresponsivity of one or two orders of magnitude higher, suggesting that the single step used in this work eliminates contaminations. Also, it is worth noting that even though we defined our MoTe₂/MoS₂ heterostructure as a photodiode, the responsivity (R) can still be larger than 1 A/W [49]. We attribute such good behavior to the almost seamless contact of the upper layer MoTe₂

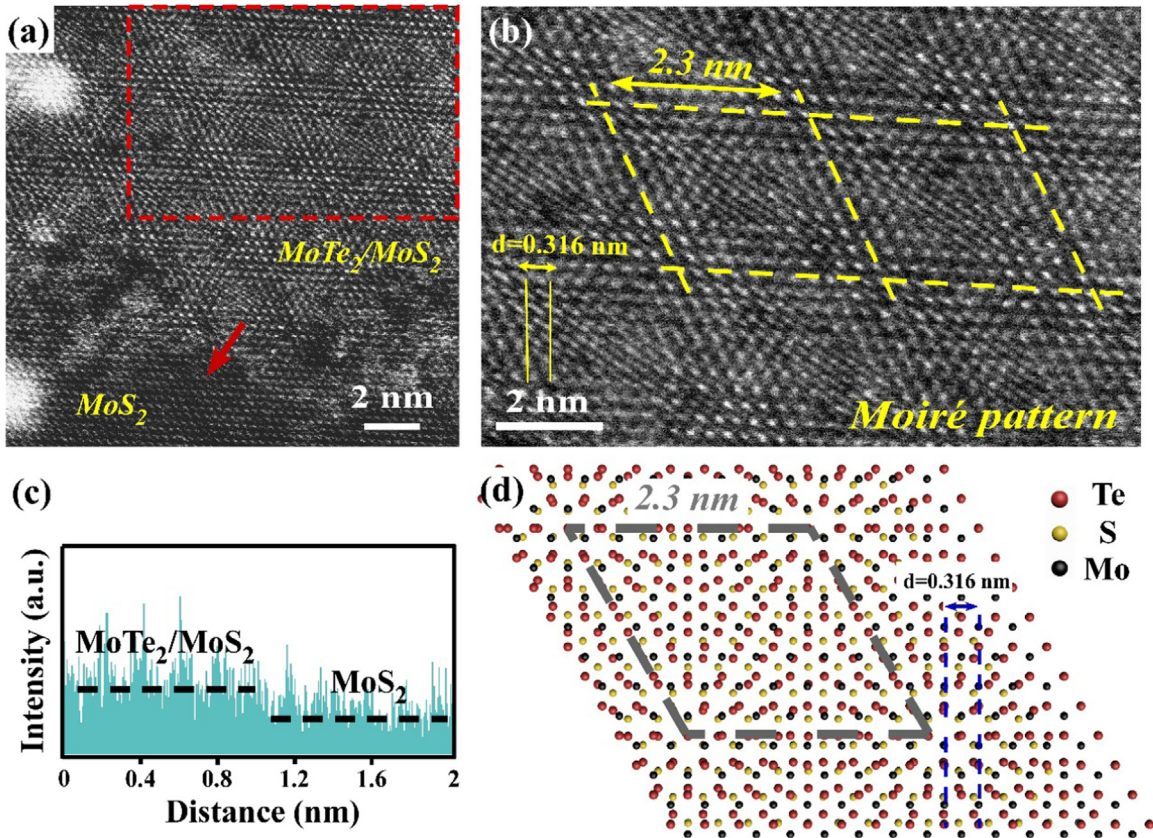


Fig. 4. Moiré patterns in MoTe₂/MoS₂ heterostructures. (a) atomic-resolution Z-contrast STEM image of the junction area. The two left light patterns are due to the charge aggregation during STEM characterization. (b) zoom in Z-contrast image of the red dash rectangle in (a). The yellow dash rhombus indicates the periodical Moiré pattern. The periodical length is around 2.3 nm. (c) Image intensity profile acquired along the red arrow in (b). (d) schematic top view of the MoTe₂/MoS₂ atomic heterostructures. The gray dash lines represent one periodical Moiré pattern.

and the under layer MoS₂ created by the one-step CVD method. In addition, a very recent theoretic report shows that [35] the stacking modes rather than the interlayer distance plays the most important role in the interlayer charge transfer for bilayer heterostructures. Therefore, the performance of our heterostructures can prove the above calculation results that this stacking-mode, confined-growth approach can result in a high photovoltaic performance for the heterostructures due to the 2H-stacks between the upper and under layers. This ultrafast transfer of the electrons and holes enables the high responsivity and external quantum efficiency in the MoTe₂/MoS₂ heterostructures [37]. Besides, compared with the pure silicon p-n diode [19] which has a bandgap of 1.12 eV, our MoTe₂/MoS₂ p-n diodes have a much higher responsivity than in the ultraviolet region, which means it holds promise for future photovoltaic applications. Fig. 5b illustrates the photo-induced current-voltage (I-V) curves of the bilayer layer MoTe₂/MoS₂ heterostructures device that was illuminated under 300, 600, 800, 1100 nm lasers and in a dark environment. Other wavelengths lasers from 200 nm to 1100 nm, at 100 nm intervals were also used to illuminate our device (details in Fig. S9). Generally, compared with the dark environment, the device showed a clear photovoltaic p-n junction effect under a forward and reverse bias voltage for all kinds of incidentals lights. The photocurrent at the forward bias shows larger changes at different illumination wavelengths, compared with that for the reverse bias. This is similar to the previous report [23,50]. Here, as we used a light splitter to separate the whole wavelength white light into different wavelength lasers, the light power density for different wavelengths cannot exactly be the same experimentally. Nonetheless, they are still in the similar order of magnitude (Table S1). The rectification of the p-n diode under various light wavelength is shown in Fig. S13, from which it can be observed that the open-circuit voltage (V_{oc})

of ~ -0.4 V was obtained under 300 nm illumination and ~ -0.2 V under 1100 nm. The short circuit current (I_{sc}) was ~ 2 pA under 300 nm illumination and ~ 0.7 pA under 1100 nm. As we discussed above in Fig. 2i, the p-type MoTe₂ and n-type MoS₂ can form a staggered gap (type II) due to the energy band alignment. Such a type II heterostructure would form a barrier at the interface due to the difference in the Fermi levels of the materials. Under illumination, photo-generated electron-hole pairs could be quickly separated at the interface with the help of a barrier. Compared with lateral epitaxial grown heterostructures or transfer-fabricated vertical heterostructures, our CVD-grown p-MoTe₂/n-MoS₂ heterostructures have larger contact areas and a much cleaner interface. Therefore, a better excitons separation efficiency can be expected. In other words, a high level of responsivity can be acquired.

Based on the above photo-induced I-V characteristics, illuminations with a 300 nm laser were further performed to study the photovoltaic characterizations under various power intensities. Here, for testing we chose 300 nm as the illumination level as it is the highest photo-induced current among all the wavelengths. The dynamic photovoltaic switching tests with a time interval of around 100 s under 2 V were conducted to test the cyclability of the photodetector. As shown in Fig. 5c, the photo-induced current increases as the light power density increases. The dependent curves of photocurrent (I_{ph}) versus light power intensity (P) with a power law [38] ($I_{ph} \propto P^\alpha$; where α is in the range of 0 ~ 1) are plotted in Fig. 5c. Here, the values of α were fitted to be ~ 0.89 , indicating the high quality of the heterostructures with very few defects or traps [38]. For the switching test, the enhancement of photocurrent under 300 nm illumination shows an on/off ratio of 5. The rise (t_r) and decay times (t_d) were also calculated, as shown in Fig. S10 and S11. Compared with the exfoliated

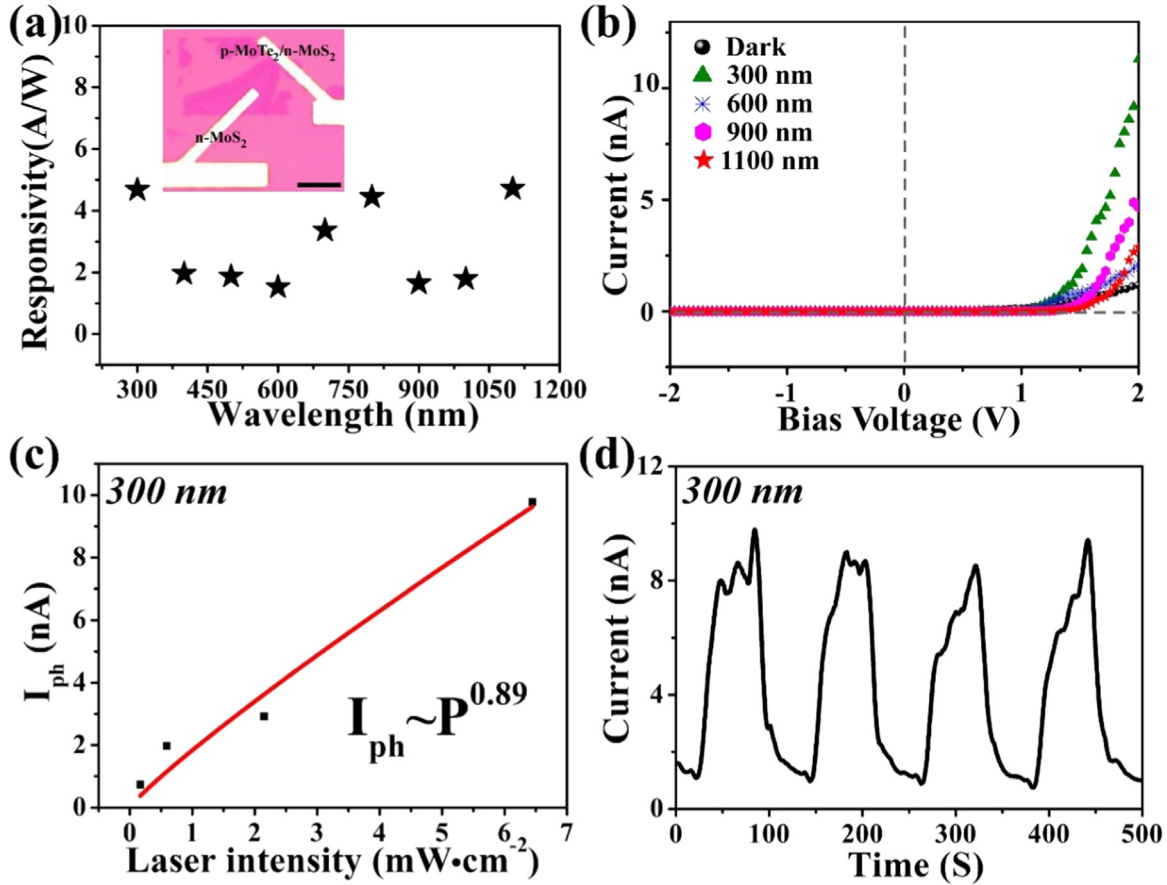


Fig. 5. Optoelectronic properties of the MoTe₂/MoS₂ heterostructures. (a) Spectral responsivity curve of the MoTe₂/MoS₂ heterostructures from 300 nm to 1100 nm illuminations calculated according to data in Table S1, with an interval of 100 nm. Inset: Optical image of the MoTe₂/MoS₂ heterostructures phototransistor on SiO₂, scale bar, 10 μm. (b) I-V curves of the device illuminated with incident light of 300, 600, 900, 1100 nm and in the dark. All the laser size is a round shape of 2 mm in diameter. (c) Photocurrent as a function of light intensity and corresponding fitting curve according to the power law. (d) On-off switching tests under 300 nm illumination for the MoTe₂/MoS₂ heterostructures phototransistor.

heterostructures, the rise and decay times are longer, which is probably the result of unavoidable extrinsic charge traps from the SiO₂ surface states or from atmospheric contamination [39]. In addition, more trapping centers induced by the partial etching operation during the device fabrication steps can also result in longer rise and decay times [51]. Moreover, in our case, the relatively slow response rate could be attributed to the configuration of our vertical heterostructure-based device: one electrode has to deposit directly on the surface of the heterojunction area, which would inevitably influence the formation of the transport barrier at the interface and further compress the effective p-n

junction area. That is, the electrodes that are on the junction area can interfere with the formation of the built-in electronic field at the interface [52]. As a result, to some degree, the role of heterostructures in the whole device is suppressed. However, the responsivity (4.71 mA/W) and the EQE (532%) of our photodetector under the 1100 nm (IR) laser was considerably larger than the previous exfoliated MoTe₂/MoS₂ heterostructures (responsivity was 38 mA/W and EQE was 6% for the highest, under 800 nm). Therefore, this indicates that, compared with the existing reports, our method is an improved approach in obtaining the MoTe₂/MoS₂ photodetectors at a much higher gain.

Table 1

Comparison of the photovoltaic properties for this work and other current 2D vdWs p-n diodes.

Ref. ^a	Materials	Method	Max. ^b Responsivity [A/W] /Wavelength [nm]	Bias voltage (V)	EQE [%]
This Work	SL n-MoS ₂ /SL p-MoTe ₂	One-step CVD	4.71/1100	2	1935
Ref [19].	Multilayer(ML) n-MoS ₂ /ML p-MoTe ₂	Exfoliated	0.32/470	5	85
Ref [20].	ML n-MoS ₂ /ML p-MoTe ₂	Exfoliated	0.064/473	2	–
Ref [41].	ML MoTe ₂	Exfoliated	0.05/637	2	–
Ref [42].	ML p-MoTe ₂ /Graphene	Exfoliated	0.02/532	2	–
Ref [43].	ML n-MoS ₂ /ML p-MoTe ₂	Exfoliated	0.15/633	1	39.4
Ref [44].	Single-layer (SL) n-MoS ₂ /SL p-WSe ₂	Exfoliated	0.12/532	20	34
Ref [45].	ML n-MoS ₂ /ML p-WSe ₂	Exfoliated	0.24/470	20	–
Ref [46].	SL n-MoS ₂ /ML p-Black phosphorus (BP)	CVD (MoS ₂) and Exfoliated (BP)	3.54/633	2	0.3
Ref [47].	SL Graphene/ML n-MoS ₂ /SL Graphene	CVD (Graphene) and Exfoliated	0.22/488	1	55
Ref [54].	SL n-SnS ₂ /SL p-WSe ₂	Two-step CVD	0.109/520	5	–
Ref [56].	SL n-MoS ₂ /SL Graphene	CVD (MoS ₂) and CVD (Graphene)	0.014/405	1	4.3

^a Ref.: Reference.

^b Max.: Maximum.

3. Conclusion

In summary, we fabricated highly crystalline ultrathin p-MoTe₂/n-MoS₂ vertically stacked heterostructures using a single-run CVD method. The successful formation of the MoTe₂/MoS₂ heterostructures was confirmed with the use of Raman, PL, and HAADF-STEM characterizations. Epitaxial MoTe₂ was revealed *in situ* growing on the top and along the edges of MoS₂ with a 2H-stacking mode, which significantly improved the contact and cleanness of the interface of the MoTe₂/MoS₂ heterostructures. As a result, photodetectors constructed from such heterostructures demonstrated a wide response range from UV to infrared. In particular, a high responsivity of 4.71 A/W (1100 nm) and a remarkable EQE of 1.935×10^{-3} (300 nm) have been recorded, which are superior to most other TMDs heterostructures reported so far. In principle, this method has the potential to enable the seamless integration of other TMDs (MoS₂, MoSe₂, WS₂, etc.). Thus, the facile synthetic strategy along with the high quality and performance of TMDs heterostructures lend themselves to the development of the next generation of photodetectors and other optoelectronic devices.

4. Experimental section

4.1. CVD synthesis of MoTe₂/MoS₂ heterostructures

Molybdenum Trioxide (MoO₃, 99.75%, Sigma Aldrich, 20 mg) was used as the molybdenum precursor and placed in a homemade quartz boat with one side open and the other side closed, and loaded at the hot center zone but in the downstream. A SiO₂/Si wafer was used as the growth substrate and placed in front of the quartz boat. The silica substrate (300 nm SiO₂/Si, 1 cm × cm) was spin-coated with the sodium cholate hydrate (SC) solution (0.1–1 wt%) as the promotor for 2D material growth. Two separate quartz boats with 3 mg sulfur and 70 mg tellurium powder (99.997%, Sigma Aldrich) were respectively located at the upstream and at a distance of 12 cm from the substrate. Both the sulfur and tellurium powder were taken out of the heating area of the furnace before growth. Sulfur will melt when the temperature of the center hot zone reaches 780 °C. Argon gas was used as the carrier gas, and hydrogen gas was only charged in during the growth of MoTe₂ to protect the system from oxidation. A magnet was attached to the tellurium boat with a quartz rod to move the boat in and out of the heating zone.

4.2. Sample characterization

The Raman/PL spectra are studied using a Confocal Raman Spectrometer (WITec Alpha 300 R), which is equipped with the UHTS 300 spectrograph (600 lines per mm grating) and a CCD detector (Andor, DU401A-BV-352). The excitation source used in this study is an air-cooled solid state laser with an excitation wavelength of 532 nm and a power of 50 mW. Mapping conditions are as follows: 100 × objectives lens with a 0.3 μm step in both the x and y axes; AFM images taken under a tapping mode with 512 resolution by Bruker Dimension Icon scanning probe microscope (Bruker Co., Germany); and the SEM images collected by a JSM-7100F (JEOL) system with a Schottky field-emission gun, 1.1 nm at 15 kV.

4.3. Sample preparation for HAADF-STEM characterization

To prepare the STEM specimen, we transferred the synthesized MoTe₂/MoS₂ heterostructures onto Cu grids using a conventional poly (methyl methacrylate) (PMMA)-based wet transfer method [40]. The substrate with the sample was spin-coated with PMMA and baked at 60 °C for 3 min. Then it was immersed in 1 M potassium hydroxide (KOH) solution at 90 °C to etch the underlying SiO₂/Si substrate. The floating PMMA/sample films in the KOH solution were transferred into deionized (DI) water and scooped with a TEM grid (a lacey carbon

film coated on 300-meshed Cu grid). The grids were then immersed into acetone for 10–15 min to remove the PMMA films and annealed in the tube furnace for 2 h at 200 °C with 100 sccm N₂ and 5 sccm H₂ as annealing gases. The crystal structures are characterized by high-resolution transmission electron microscopy (HRTEM, JEM-2100). HAADF-STEM analysis is characterized using a JEM Titan G2 60–300 TEM (JEOL) with 60–300 kV.

4.4. Photovoltaic device fabrication and characterization

For the MoTe₂/MoS₂ heterostructures device, electrodes were fabricated by electron beam lithography (Nexdep, Angstrom Engineering). To electrically access the inner MoS₂ triangles without shorting to the outer MoTe₂ peripheral layers, the partial etching of the MoTe₂/MoS₂ heterostructures was prepared in advance before writing the electrodes. A thin film of PMMA was firstly spin-coated onto the as-received sample. After this initial exposure, only half of the wanted flakes was protected by PMMA while the rest was lifted off by lithography. After this, electrodes were made by EBL and followed by depositing 10 nm Cr/50 nm Au thin films using thermal evaporation (Nexdep, Angstrom Engineering). Then the devices were annealed at 200 °C inside a vacuum furnace to enhance the contact between the materials and the metal electrode. For photodetection, laser-driven light sources (EQ-1500, Energetiq) were used, which were calibrated by a silicon photodiode to provide incidental light. A time-resolved photocurrent was collected using a current meter. The quick response was recorded with a semiconductor characterization system measured on (B1500A, Agilent) under illumination of 300 nm and 800 nm light pulses chopped at a frequency of 1 Hz. All the measurements were performed in air and under room temperature.

Acknowledgements

We thank Professor Ping Shen at the Hong Kong University of Science and Technology for his input and assistance. This project was supported by the Research Grant Council of Hong Kong SAR (RGC, Project number 16204815), National Natural Science Foundation of China (NNSFC, 91622117, 51727809), NSFC-RGC Joint Research Scheme (N_HKUST607/17) and the Guangzhou Science & Technology Project (2016201604030023 and 201704030134). We appreciate support from the Center for 1D/2D Quantum Materials, State Key Laboratory on Advanced Displays and Optoelectronics at HKUST and the Innovation and Technology Commission of Hong Kong (ITS/267/15 and ITC-CNERC14SC01). Technical assistance from the Materials Characterization and Preparation Facilities is greatly appreciated. We also acknowledge funding from the National Natural Science Foundation of China (No.11474147), the National Basic Research Program of China (Grant No. 2015CB654901) and the Natural Science Foundation of Jiangsu Province (Grant No. BK20151383).

Appendix A. Supporting information

Supplementary data associated with this article can be found in the online version at <http://dx.doi.org/10.1016/j.nanoen.2018.04.055>.

References

- [1] C. Tan, P. Yu, Y. Hu, J. Chen, Y. Huang, Y. Cai, Z. Luo, B. Li, Q. Lu, L. Wang, J. Am. Chem. Soc. 137 (2015) 10430–10436.
- [2] D.H. Keum, S. Cho, J.H. Kim, D.-H. Choe, H.-J. Sung, M. Kan, H. Kang, J.-Y. Hwang, S.W. Kim, H. Yang, Nat. Phys. 11 (2015) 482–486.
- [3] X. Duan, C. Wang, J.C. Shaw, R. Cheng, Y. Chen, H. Li, X. Wu, Y. Tang, Q. Zhang, A. Pan, Nat. Nanotechnol. 9 (2014) 1024–1030.
- [4] M. Yankowitz, J. Xue, D. Cormode, J.D. Sanchez-Yamagishi, K. Watanabe, T. Taniguchi, P. Jarillo-Herrero, P. Jacquod, B.J. LeRoy, Nat. Phys. 8 (2012) 382–386.
- [5] B. Hunt, J. Sanchez-Yamagishi, A. Young, M. Yankowitz, B.J. LeRoy, K. Watanabe, T. Taniguchi, P. Moon, M. Koshino, P. Jarillo-Herrero, Science 340 (2013)

- 1427–1430.
- [6] C. Woods, L. Britnell, A. Eckmann, R. Ma, J. Lu, H. Guo, X. Lin, G. Yu, Y. Cao, R. Gorbachev, Nat. Phys. 10 (2014) 451–456.
- [7] A.K. Geim, I.V. Grigorieva, Nature 499 (2013) 419–425.
- [8] W. Yang, G. Chen, Z. Shi, C.-C. Liu, L. Zhang, G. Xie, M. Cheng, D. Wang, R. Yang, D. Shi, Nat. Mater. 12 (2013) 792–797.
- [9] Y. Gong, S. Lei, G. Ye, B. Li, Y. He, K. Keyshar, X. Zhang, Q. Wang, J. Lou, Z. Liu, Nano Lett. 15 (2015) 6135–6141.
- [10] Y.-C. Lin, R.K. Ghosh, R. Addou, N. Lu, S.M. Eichfeld, H. Zhu, M.-Y. Li, X. Peng, M.J. Kim, L.-J. Li, Nat. Commun. 6 (2015) 7311.
- [11] Y. Gong, J. Lin, X. Wang, G. Shi, S. Lei, Z. Lin, X. Zou, G. Ye, R. Vajtai, B.I. Yakobson, Nat. Mater. 13 (2014) 1135–1142.
- [12] C. Ruppert, O.B. Aslan, T.F. Heinz, Nano Lett. 14 (2014) 6231–6236.
- [13] C.H. Naylor, W.M. Parkin, J. Ping, Z. Gao, Y.R. Zhou, Y. Kim, F. Streller, R.W. Carpick, A.M. Rappe, M. Drndic, Nano Lett. 16 (2016) 4297–4304.
- [14] Y. Gong, Z. Lin, G. Ye, G. Shi, S. Feng, Y. Lei, A.L. Elías, N. Perea-Lopez, R. Vajtai, H. Terrones, ACS Nano 9 (2015) 11658–11666.
- [15] F. Cui, C. Wang, X. Li, G. Wang, K. Liu, Z. Yang, Q. Feng, X. Liang, Z. Zhang, S. Liu, Adv. Mater. 28 (2016) 5019–5024.
- [16] B. Chen, H. Sahin, A. Suslu, L. Ding, M.I. Bertoni, F. Peeters, S. Tongay, ACS Nano 9 (2015) 5326–5332.
- [17] Q. Fang, Z. Zhang, Q. Ji, S. Zhu, Y. Gong, Y. Zhang, J. Shi, X. Zhou, L. Gu, Q. Wang, Y. Zhang, Nano Res. DOI: 10.1007/s12274-017-1480-z.
- [18] H.C. Diaz, R. Chaghi, Y. Ma, M. Batzill, 2D Mater. 2 (2015) 044010.
- [19] A. Pezeshki, S.H.H. Shokouh, T. Nazari, K. Oh, S. Im, Adv. Mater. 28 (2016) 3216–3222.
- [20] F. Wang, L. Yin, Z.X. Wang, K. Xu, F.M. Wang, T.A. Shifa, Y. Huang, C. Jiang, J. He, Adv. Funct. Mater. 26 (2016) 5499–5506.
- [21] K.-A.N. Duerloo, E.J. Reed, ACS Nano 10 (2015) 289–297.
- [22] L. Zhang, K. Liu, A.B. Wong, J. Kim, X. Hong, C. Liu, T. Cao, S.G. Louie, F. Wang, P. Yang, Nano Lett. 14 (2014) 6418–6423.
- [23] M.-Y. Li, Y. Shi, C.-C. Cheng, L.-S. Lu, Y.-C. Lin, H.-L. Tang, M.-L. Tsai, C.-W. Chu, K.-H. Wei, J.-H. He, Science 349 (2015) 524–528.
- [24] L. Zhou, K. Xu, A. Zubair, A.D. Liao, W. Fang, F. Ouyang, Y.-H. Lee, K. Ueno, R. Saito, T. s. Palacios, J. Am. Chem. Soc. 137 (2015) 11892–11895.
- [25] J.C. Park, S.J. Yun, H. Kim, J.-H. Park, S.H. Chae, S.-J. An, J.-G. Kim, S.M. Kim, K.K. Kim, Y.H. Lee, ACS Nano 9 (2015) 6548–6554.
- [26] C. Rice, R. Young, R. Zan, U. Bangert, D. Wolverson, T. Georgiou, R. Jalil, K. Novoselov, Phys. Rev. B 87 (2013) 081307.
- [27] W. Novoselov, D. Bullett, J. Phys. Condens. Matter 20 (1987) 6159.
- [28] D. Chiappe, E. Scalise, E. Cinquanta, C. Grazianetti, B. van den Broek, M. Fanciulli, M. Houssa, A. Molle, Adv. Mater. 26 (2014) 2096–2101.
- [29] K. Zhang, S. Hu, Y. Zhang, T. Zhang, X. Zhou, Y. Sun, T.-X. Li, H.J. Fan, G. Shen, X. Chen, ACS Nano 9 (2015) 2704–2710.
- [30] H. Guo, T. Yang, M. Yamamoto, L. Zhou, R. Ishikawa, K. Ueno, K. Tsukagoshi, Z. Zhang, M.S. Dresselhaus, R. Saito, Phys. Rev. B 91 (2015) 205415.
- [31] Y. Zhou, E.J. Reed, J. Phys. Chem. C 119 (2015) 21674–21680.
- [32] Y.H. Lee, X.Q. Zhang, W. Zhang, M.T. Chang, C.T. Lin, K.D. Chang, Y.C. Yu, J.T.W. Wang, C.S. Chang, L.J. Li, Adv. Mater. 24 (2012) 2320–2325.
- [33] K. Zhang, T. Zhang, G. Cheng, T. Li, S. Wang, W. Wei, X. Zhou, W. Yu, Y. Sun, P. Wang, ACS Nano 10 (2016) 3852–3858.
- [34] J. Yuan, S. Najmaei, Z. Zhang, J. Zhang, S. Lei, P.M. Ajayan, B.I. Yakobson, J. Lou, ACS Nano 9 (2015) 555–563.
- [35] J. Zhang, H. Hong, C. Lian, W. Ma, X. Xu, X. Zhou, H. Fu, K. Liu, S. Meng, Adv. Sci. 4 (2017) 1700086.
- [36] X. Li, M.-W. Lin, J. Lin, B. Huang, A.A. Puretzky, C. Ma, K. Wang, W. Zhou, S.T. Pantelides, M. Chi, Sci. Adv. 2 (2016) e1501882.
- [37] S. Pan, F. Ceballos, M.Z. Bellus, P. Zereshki, H. Zhao, 2D Mater. 4 (2016) 015033.
- [38] M. Hafeez, L. Gan, H. Li, Y. Ma, T. Zhai, Adv. Mater. 28 (2016) 8296–8301.
- [39] J.D. Mehew, S. Unal, E. Torres Alonso, G.F. Jones, S. Fadhil Ramadhan, M.F. Craciun, S. Russo, Adv. Mater. DOI: 10.1002/adma.201700222.
- [40] Y. Ding, Q. Peng, L. Gan, R. Wu, X. Ou, Q. Zhang, Z. Luo, Chem. Mater. 28 (2016) 1034–1039.
- [41] H. Huang, J. Wang, W. Hu, L. Liao, P. Wang, X. Wang, F. Gong, Y. Chen, G. Wu, W. Luo, Nanotechnology 27 (2016) 445201.
- [42] M. Kuiri, B. Chakraborty, A. Paul, S. Das, A. Sood, A. Das, Appl. Phys. Lett. 108 (2016) 063506.
- [43] B. Wang, S. Yang, C. Wang, M. Wu, L. Huang, Q. Liu, C. Jiang, Nanoscale 9 (2017) 10733–10740.
- [44] C.-H. Lee, G.-H. Lee, A.M. Van Der Zande, W. Chen, Y. Li, M. Han, X. Cui, G. Arefe, C. Nuckolls, T.F. Heinz, Nat. Commun. 9 (2014) 676–681.
- [45] P.J. Jeon, S.-W. Min, J.S. Kim, S.R.A. Raza, K. Choi, H.S. Lee, Y.T. Lee, D.K. Hwang, H.J. Choi, S. Im, J. Phys. Chem. C 3 (2015) 2751–2758.
- [46] Y. Deng, Z. Luo, N.J. Conrad, H. Liu, Y. Gong, S. Najmaei, P.M. Ajayan, J. Lou, X. Xu, P.D. Ye, ACS Nano 8 (2014) 8292–8299.
- [47] W.J. Yu, Y. Liu, H. Zhou, A. Yin, Z. Li, Y. Huang, X. Duan, Nat. Nanotechnol. 8 (2013) 952–958.
- [48] C. Gong, H. Zhang, W. Wang, L. Colombo, R.M. Wallace, K. Cho, Appl. Phys. Lett. 103 (2013) 053513.
- [49] a) H. Zhang, X. Zhang, C. Liu, S.-T. Lee, J. Jie, ACS Nano 10 (2016) 5113; b) L. Ye, H. Li, Z. Chen, J. Xu, ACS Photonics 3 (2016) 692.
- [50] C.O. Kim, S. Kim, D.H. Shin, S.S. Kang, J.M. Kim, C.W. Jang, S.S. Joo, J.S. Lee, J.H. Kim, S.-H. Choi, Nat. Commun. 5 (2014) 3249.
- [51] Y. Xue, Y. Zhang, Y. Liu, H. Liu, J. Song, J. Sophia, J. Liu, Z. Xu, Q. Xu, Z. Wang, ACS Nano 10 (2015) 573.
- [52] K.H. Lee, T.H. Kim, H.J. Shin, S.W. Kim, Adv. Mater. 28 (2016) 1793.
- [53] Z. Tu, G. Li, X. Ni, L. Meng, S. Bai, X. Chen, J. Lou, Y. Qin, Appl. Phys. Lett. 109 (2016) 223101.
- [54] T. Yang, B. Zheng, Z. Wang, T. Xu, C. Pan, J. Zou, X. Zhang, Z. Qi, H. Liu, Y. Feng, W. Hu, F. Miao, L. Sun, X. Duan, A. Pan, Nat. Commun. 8 (2017) 1906.
- [55] A. Stesmans, B. Nouwen, V.V. Afanas'ev, Phys. Rev. B 66 (2002) 045307.
- [56] H. Henck, D. Pierucci, J. Chaste, C.H. Naylor, J. Avila, A. Balan, M.G. Silly, M.C. Asensio, F. Sirotti, A.T.C. Johnson, E. Lhuillier, A. Ouerghi, Appl. Phys. Lett. 109 (2016) 113103.